Article

Molecular Origin of the Sign Preference of Ion- Induced Heterogeneous Nucleation in a Complex Ionic Liquid−Diethylene Glycol System

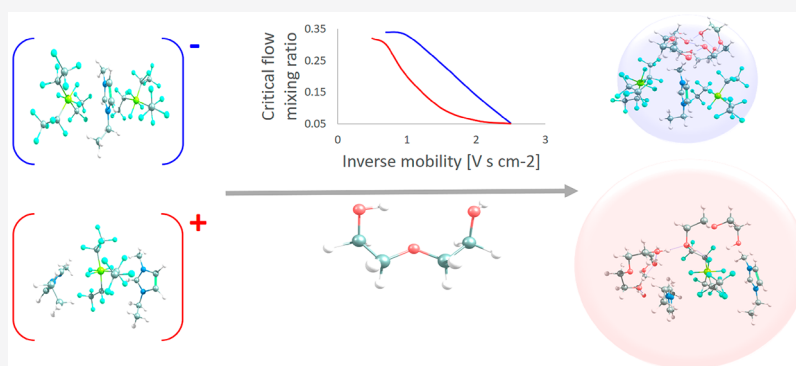Fatemeh Keshavarz,*,# Jakub Kubečka, Michel Attoui, Hanna Vehkamäki, Theo Kurtén, and Juha Kangasluoma*,#

ACCESS | Metrics & More | Article Recommendations | SI Supporting Information

ABSTRACT: Heterogeneous nucleation on charged seeds has been shown to frequently prefer a given sign of electrical charge (anion or cation), at constant seed size and (apparent) chemical composition. For some systems, this sign preference can be readily understood in terms of individual chemical interactions. However, experiments are in general unable to provide satisfying molecular-level explanations for the sign preference of chemically complex systems. Here, we experimentally demonstrate a positive sign preference for charged ionic liquid seeds (CILS) with diethylene glycol vapor (DEG) and explain the physicochemical origins of this preference via quantum chemical calculations. The computational results show that all enthalpies and free energies for adsorption of DEG onto the CILS clusters are lower for the positively charged seeds compared to those for the negatively charged seeds. The main reason for this difference is the stronger hydrogen bonds in the cationic clusters originating from the ability of imidazolium-based cations to act as hydrogen bond acceptors.

INTRODUCTION

Heterogeneous nucleation is a phase change process in which a new phase forms onto an existing seed. These processes are important, for example, in material sciences,[1−4] in atmospheric cloud and ice nuclei formation,[5−7] and for fundamental understanding of physics and chemistry.[8−10] In the specific case of gas-to-particle conversion, new solid particles or liquid droplets form via heterogeneous nucleation and subsequent condensation of vapors. Heterogeneous nucleation is governed by the interactions between the seed and the condensing vapor, which are affected by the size, charging state and chemical composition of the seed,[11−14] supersaturation and chemical composition of the vapor,[15,16] and nucleation temperature.[17,18]

Classical theoretical treatment of heterogeneous nucleation is based on the Kelvin equation for neutral seeds and the Kelvin−Thomson model for charged seeds. The latter model does not distinguish between positive and negative charges. Both theories incorporate bulk properties of the seeds and
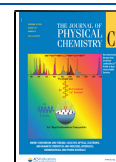
vapor to treat molecular-level processes. Several experiments have tested these theories, often finding the critical supersaturation required for a chosen threshold particle formation rate to be lower than the theoretically predicted one.[16,18−24] On the other hand, Tauber et al.[14] has reported ion-induced nucleation experiments on singly charged atoms, which follow well the Kelvin−Thomson prediction.

An unresolved question in the process of heterogeneous nucleation is the interlinked roles of electric charge and seed chemical composition. More than a hundred years ago, Wilson[25] conducted cloud chamber experiments by condens-

ing water vapor onto unipolar ionic seeds, noting that cloud formation takes place more readily when negative ions are present in the chamber compared to when positive ions are present. This observation has been called "negative sign preference". After Wilson, several experiments reported negative or positive sign preferences in various systems. In some of them, small ions were produced in a chamber, and the number of nucleated particles was counted after the ions were exposed to supersaturated vapor.[26−31] Such techniques lack control over ion size as well as seed chemistry. Other experiments produced ions of controlled size and charging state using differential mobility analysis (DMA) and probed the heterogeneous nucleation probability as a function of seed size. Also, such experiments have reported more significant seed activation at constant seed size at one polarity compared to the other polarity, indicative of sign preference.[14,22,23,32−34]

The effect of the vapor chemical composition has been studied more than the chemical composition of the seed likely because of the lack of experimental and computational methods capable of treating the complexity of the seed accurately. Through use of mass spectrometric techniques for seed characterization, it was recently shown that seeds formed from the same source material but with different polarities do not necessarily have the same chemical composition because of the presence of impurities and/or differences in the chemical reactions forming them.[35,36] This observation highlights the challenge of distinguishing the effect of seed composition from that of the charging state without direct measurement of the cluster composition, as discussed also in the theoretical study of Kathmann et al.[37] Other theoretical examinations of sign preference have, for example, found that negative pure water clusters nucleate more readily than the positive ones,[38] while sulfuric acid−water clusters display a strong negative sign preference.[39] The latter can be explained in terms of acid−base interactions: strong acids such as sulfuric acid prefer anionic clusters since anions act as bases.[40] What is quite well experimentally established is that charged seeds, especially at cluster sizes of a few nanometers, are generally preferred over neutral seeds for nucleation;[11,12,41] However, computational studies suggest a few exceptions even to this rule: for example, H_2SO_4 prefers neutral amines over protonated aminium cations,[40] again because of greater basicity of the neutral molecule. Apart from these exceptional cases of strong acids and/or strong bases, our understanding of the molecular origins behind the sign preferences observed for specific chemistries and charging states, especially in complex systems, remains limited.

Here, we explain the experimentally observed heterogeneous nucleation sign preference of a chemically complex system through first-principles quantum chemical modeling. We study the first steps of diethylene glycol (DEG) nucleation on singly charged clusters of 1-butyl-3-methyl imidazolium tetraboroflorate ($C_8N_2H_{15}BF_4$, BMIBF$_4$), 1-ethyl-3-methylimidazolium tris(pentafluoroethyl)trifluorophosphate ($C_6N_2H_{11}(C_2F_5)_3PF_3$, EMIFAP), and 1-ethyl-3-methylimidazolium trifluoromethanesulfonate ($C_6N_2H_{11}CF_3SO_3$, EMITFMS) ionic liquids (ILs; Figure S1, Supporting Information) of the $(AC)_nA^-$ or $(AC)_nC^+$ type (A, anion; C, cation). We have selected this system for our theoretical study, as the exact chemical composition of these clusters can be determined experimentally.

METHODS

Experimental Measurement. For generation of the seeds, the ILs were dissolved in methanol and the resultant 20 mM solutions were electrosprayed using a bipolar electrospray source (Fernandez de la Mora and Barrios-Collado 2017). The two needles were flushed with particle-free compressed air at a flow rate of 6 L min^{-1}, and mobilities and cross sections were measured in air at 101325 Pa and 298 K. The generated polydisperse cloud of ions in the sample flow was guided into a Half-mini p-type differential mobility analyzer (DMA; Fernández de la Mora 2017) to separate a close to monomobile unipolar ion distribution from the initial sample. The absolute ion concentration was measured downstream of the DMA using an aerosol electrometer with a flow rate of 2.5 L min^{-1}, and parallel to that the flow reactor was operated with an equal inlet flow of 2.5 L min^{-1}. The reactor was a two-stage commercial mixing type condensation particle counter Airmodus A11 (Vanhanen et al. 2011), typically called a particle size magnifier (PSM). In the first stage, the aerosol flow was adiabatically and turbulently mixed with a heated flow that was saturated with diethylene glycol, DEG, to create DEG supersaturation. The operational temperatures were as follows: saturator 82 °C, growth tube 2 °C, and inlet 40 °C. The DEG flow rate was scanned from 0.1 to 1.3 L min^{-1} to vary the supersaturation level. The particles that were grown by DEG reached the size of about 90 nm, and they were further enlarged by butanol condensation and finally counted by an optical detector. The supersaturation level of the reactor was scanned in a 2 min cycle for each selected ion mobility from 0% to 100% activation probability. The described experimental setup is schematically shown in Figure S2. For plotting of Figures 2 and 3, the data were selected to present just the clusters with activation probabilities close to 100% at the highest supersaturation (filtering out the very small clusters), and no background counts were detected at the lowest supersaturation, originating likely from multiply charged ions overlapping with sample clusters (filtering out the large clusters).

Because of the complex structure of the reactor, the exact determination of the supersaturation level was uncertain, and we used the flow mixing ratio, calculated as $Q_s/(Q_s + Q_a)$, where Q_s is the saturated flow rate and Q_a the aerosol flow rate, as a trace for supersaturation. This is sufficient for examining the sign preference. The heterogeneous nucleation probability was obtained as the ratio of particle concentration detected by the PSM to the concentration detected by the aerosol electrometer. The critical flow mixing ratio required for nucleation was determined as the flow mixing ratio giving 50% probability of heterogeneous nucleation. The critical mixing ratio was measured for CILS filling the two previous criteria (of ca. 100% nucleation probability and detection of no background counts) for both polarities of the three ILs by varying the selected mobility in the mobility analyzer. Sign preference was identified as the smaller critical mixing ratio between positive and negative seeds.

The classification voltages of the DMA were translated to collision cross sections (CCSs) using the Mason−Schamp equation

$$CCS = \frac{3}{16} \sqrt{\frac{2\pi}{\mu k_B T}} \frac{ze}{N_0 Z_0}$$

(1)

where $\mu = m_i m_g/(m_i + m_g)$ is the reduced mass, k_B is Boltzmann's constant, T is temperature (298 K), z is the charging state, e is unit charge, N_0 is Loschmidt number, and Z_0 is the reduced mobility given by

$$Z_0 = Z\frac{p}{p_0}\frac{T_0}{T} \tag{2}$$

where T_0 is 273.15 K, T is 298 K, p_0 is 100000 Pa, p is 101325 Pa, and Z is the measured mobility. The voltages were translated into mobility using the relation $V_1/V_{ref} = (1/Z_1)/(1/Z_{ref})$, where Z_{ref} is the mobility of the EMI$^+$ ion taken from Larriba et al.[42] and V_{ref} is the peak voltage measured for the EMI$^+$ ion in our measurements.

Computational Modeling. The initial steps of the heterogeneous nucleation process of charged (AC)A$^-$ and (AC)C$^+$ clusters with two cations or anions of the same ionic liquids as in the experiments were modeled by DFT calculations at the ωB97X-D/6-31+g(d) and ωB97X-D/def2TZV levels by Gaussian 16 (ref 43). Our working hypothesis is that the results obtained for the (AC)A$^-$ and (AC)C$^+$ clusters can shed light on the mechanism of the nucleation process over the whole range of cluster sizes, as the individual vapor–seed interactions are likely to be similar. A corollary hypothesis is that the adsorption of the first few DEG molecules similarly provides at least qualitative insights into the overall DEG condensation process, including especially the relative differences between seeds of different compositions and charge states. This hypothesis is based on the fact that if the binding of the first few vapor molecules to a seed of some particular polarity is very weak, then the seed in question will never nucleate, as the molecules will always evaporate before further vapor molecules collide with the seed. Also, the formation free energy of the critical cluster is ultimately determined by the same types of chemical interactions (e.g., seed–vapor and vapor–vapor) already present in the small clusters with two to three vapor molecules. Thus, if enormous differences are found in the favorability of adsorption of the first vapor molecules to two different seeds, this will inevitably translate into a large difference also between the corresponding critical clusters. Therefore, the association of the first few vapor molecules with two different seeds is sufficient for determining the relative supersaturations required for heterogeneous nucleation onto those two seeds. Furthermore, this hypothesis has been previously demonstrated acceptable, for example, for the case of water condensation onto charged sulfuric acid clusters,[39] and is also supported by the similarities in the trends of the adsorption energies for the first three DEG molecules, as discussed in the results. Quantitative modeling of the heterogeneous nucleation rate or probability would require that the simulated set of clusters includes the critical cluster— which is often rendered impossible by computational limitations. As the number of DEG molecules in the critical cluster (for a given seed) depends on the supersaturation, this criterion is met for some supersaturations, even for our relatively small cluster data set. However, as we cannot directly quantify the experimental supersaturation in our setup, a quantitative comparison of modeled and experimental rates is in any case outside the scope of this study.

The first steps of heterogeneous nucleation were modeled by calculating the enthalpies and Gibbs free energies of DEG adsorption onto the clusters. Because of the presence of multiple low-lying vibrational modes, the quasi-harmonic

approximation[44−46] was used to correct for the errors in the standard rigid rotor–harmonic oscillator approximation (see Section SA of the Supporting Information). Since the rate of vapor evaporation from the clusters depends exponentially on the adsorption free energy (with lower free energies giving slower evaporation), the free energy is directly related to heterogeneous nucleation probability. In particular, if the free energy of adsorption of the first few DEG molecules to some seed are too high, leading to high evaporation rates compared to the collision rates corresponding to some given supersaturation, heterogeneous nucleation will not occur. Differences in adsorption energies of the first few vapor molecules between anion and cation seeds of similar sizes may thus be linked to the experimentally observed sign preferences. Full details of the calculations can be found in Section SA of the Supporting Information.

Briefly, the calculations started with computational level validation (Figure S3) and conformational/configurational analysis of EMI, BMI, and FAP. We used the lowest-energy gas-phase conformer of DEG in the simulations. While this introduces a minor uncertainty, we note that this conformer is well-suited for adsorption, as it has both OH groups on the same side (see Figure S5) and is able to bond to a seed. After selection of several representative anion and cation conformers/configurations (see Figure S4), a systematic configurational sampling technique[47] was used to create a total of 16 charged ionic liquid seeds (CILSs; see Section SB of the Supporting Information for more information about their conformational diversity) and CILS−DEG clusters. In this technique, a large set of seed and seed−DEG configurations was generated using low-cost calculations. Then the structures were optimized at a higher level of theory and filtered on the basis of their uniqueness and energy profiles. The re-optimization and filtering steps were repeated until we reached the global minimum structure for each cluster. After that, natural bond-orbital (NBO) analysis was performed to understand the bonding patterns of the most stable CILS−DEG clusters.

In the end, we selected the lowest energy CILSs from the quantum chemical calculations and calculated their collision cross section (CCS) using Ion Mobility Software,[48,49] which models the drag force induced by the ion-neutral collisions. In the IMOS software, we used the trajectory method with Lennard−Jones potentials and quadrupole interactions included in the collisions, using the CHelpG partial charges (CHarges from electrostatic potentials using a grid-based method) calculated at the ωB97X-D/def2TZV level and listed in Section SC of the Supporting Information. In IMOS, the Lennard−Jones (LJ) potentials have been optimized against experiments only for the collisions with N$_2$ molecules;[50] therefore, we ran the CCS simulation both in N$_2$ and air (which was the carrier gas in our experiments but for which the LJ have not been optimized). We report only the results with N$_2$ as the modeled CCSs are closer to the experimental CCS as compared to CCS modeled in air with unoptimized LJ parameters. The CCS values of the modeled CILSs were directly compared to the measured CCSs at 273 K and 100000 Pa, allowing us to both validate our structural results and also connect the modeling results on DEG absorption to a particular size range of seeds studied in the experiments.

RESULTS AND DISCUSSION

Figure 1 presents the mobility spectrum of the positively and negatively charged EMITFMS seeds. The signals from the
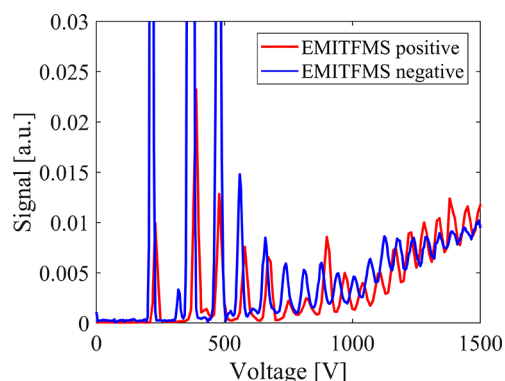

Figure 1. Mobility spectrum of EMITFMS.

individual clusters are well-separated in the mobility space, and we can thus assume that the cluster populations downstream of the DMA consist of only one cluster type. At around 700−800 V and larger voltages the oscillating signals increasingly deviate from 0 a.u., suggesting some contribution of multiply charged droplets to the measured signals. Table 1 lists the reduced mobilities Z_0 and CCSs for the ten smallest ions for each sample.

Figure 2 presents the activated fraction of the EMITFMS clusters in the flow reactor as a function of the DEG mixing ratio. Large open circles are the $n = 1$ clusters, which are further modeled for DEG adsorption. We can observe that, as expected, the larger clusters are activated at lower mixing ratios and that the positively charged clusters require smaller mixing ratios to be activated relative to the negative clusters of similar CCS (compare, for example, the open circle symbols for clusters with CCSs of 303 and 307 Å^2). This observation can be interpreted as positive sign preference in our IL-DEG system and is observed for the three different IL samples. From these data we infer the critical mixing ratio for each cluster as the mixing ratio at which the activation probability is 50%.

Figure 3 collects the critical mixing ratios for each cluster type plotted against the experimental CCSs, while Table 2 verifies the structures of the modeled CILSs by comparing the experimental and modeled CCSs and giving the maximal CCS difference of 7.31%; Table 3 reports the nucleation modeling results. In Table 3, the positive and negative CILSs contain the name of the base ionic liquid and the second anion/cation, in addition to the total charge of the seed. Similar CILSs with different cation/anion conformational/configurational compositions are distinguished by numbering them based on their Gibbs free energy (ΔG) of formation (ωb97X-D/def2TZVP level; neglecting the quasi-harmonic treatment). For instance, among the three negatively charged EMIFAP seeds, (EMIFAP)FAP$^-$-1 and (EMIFAP)FAP$^-$-3 are the most and least stable seeds, respectively.

At constant CCS, a smaller DEG mixing ratio is required for heterogeneous nucleation onto the positive seeds compared to that on the negative ones for all CILS sizes and compositions, clearly exhibiting positive sign preference in our test systems. The computed thermodynamics parameters in Table 3 generally support this, as the ΔG values clearly indicate that DEG prefers adsorption on the positively charged EMITFMS

Table 1. Experimental Masses, Reduced mobilities (Z_0, cm^2 V^{-1}) and CCSs (Å^2) for the Ten Smallest CILSs of Each Sample Based on DMA Classification Voltages[a]

	BMIBF4$^-$			BMIBF4$^+$		
ion pair	mass	CCS	Z_0	mass	CCS	Z_0
0	87.00	108.44	2.12	139.12	127.82	1.71
1	313.13	172.95	1.20	365.25	190.49	1.09
2	539.26	215.76	0.95	591.38	233.59	0.87
3	765.38	255.13	0.79	817.50	273.03	0.74
4	991.51	299.43	0.67	1043.63	317.35	0.64
5	1217.63	334.84	0.60	1269.76	348.24	0.58
6	1443.76	370.36	0.54	1495.88	379.26	0.53
7	1669.89	401.44	0.50	1722.01	414.86	0.48
8	1896.01	432.57	0.46	1948.13	446.00	0.45
9	2122.14	463.74	0.43	2174.26	472.67	0.42
	EMITFMS$^-$			EMIFTMS$^+$		
ion pair	mass	CCS	Z_0	mass	CCS	Z_0
0	148.95	117.57	1.85	111.09	115.51	1.93
1	409.00	185.17	1.11	371.14	181.09	1.14
2	669.04	223.85	0.91	631.18	224.10	0.91
3	929.08	263.40	0.77	891.22	263.55	0.77
4	1189.13	307.78	0.65	1151.27	303.36	0.66
5	1449.17	347.77	0.58	1411.31	338.82	0.59
6	1709.22	374.31	0.54	1671.36	369.86	0.54
7	1969.26	409.93	0.49	1931.40	405.48	0.49
8	2229.31	441.09	0.45	2191.45	436.63	0.46
9	2489.35	472.27	0.42	2451.49	467.81	0.43
	EMIFAP$^-$			EMIFAP$^+$		
ion pair	mass	CCS	Z_0	mass	CCS	Z_0
0	444.95	150.67	1.36	111.09	115.51	1.93
1	1000.98	249.05	0.81	667.13	210.13	0.97
2	1557.02	318.11	0.63	1223.17	305.48	0.66
3	2113.06	374.14	0.54	1779.20	411.40	0.49
4	2669.09	440.32	0.45	2335.24	474.05	0.42
5	3225.13	489.91	0.41	2891.28	560.18	0.36
6	3781.17	539.54	0.37	3447.32	599.71	0.33
7	4337.21	585.88	0.34	4003.35	639.32	0.31
8	4893.24	625.59	0.32	4559.39	682.31	0.29
9	5449.28	668.65	0.30	5115.43	722.00	0.28

[a]An ion pair number n corresponds to anions of the type (AC)$_n$A$^-$ and cations of the type (AC)$_n$C$^+$.
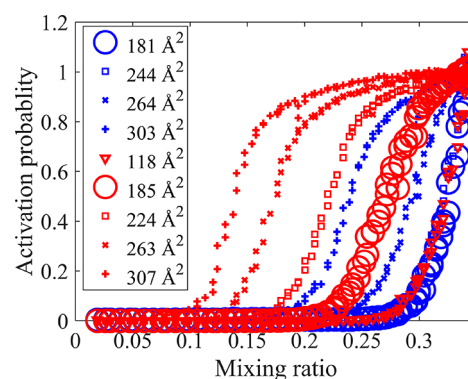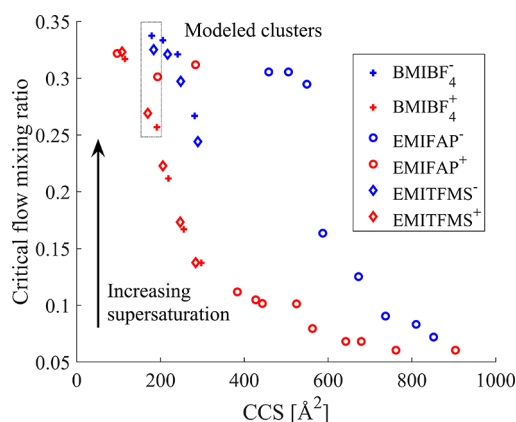

Figure 2. Activation probability as a function of the flow mixing ratio for EMITFMS. Red data is for positive clusters and blue for negative clusters. Large open circles are the clusters ($n = 1$) for which vapor adsorption modeling is conducted.

Figure 3. DEG flow mixing ratios of the CILSs as a function of the clusters' CCSs. Negative EMIFAP with $n = 1$ was also modeled even though heterogeneous nucleation was not observed for it in our experimental conditions.

and BMIBF4 seeds. In the case of EMIFAP, the adsorption energy (ΔE), enthalpy (ΔH), and ΔG values indicate only slight positive seed preference, while the experiments suggest EMIFAP shows the highest difference in mixing ratio at constant CCS (i.e., the strongest sign preference). Noteworthily, EMIFAP was quite computationally demanding and its harmonic frequency calculations yielded many low frequencies and a few imaginary vibrations (which were eliminated as described in Section SA of the Supporting Information). Therefore, the reliability of our computations is lower for EMIFAP, and the EMIFAP results are more sensitive to quasi-harmonic corrections relative to the EMITFMS and BMIBF4 CLISs.

To uncover the actual molecular-level interactions behind the patterns seen in Figure 3 and Table 3, we performed NBO analysis. Table 4 shows the key results of this analysis: $E^{(2)}$ is second-order perturbation energy, which quantifies the strength of various donor–acceptor interactions. As indicated by Table 4 and Figure S6, the main type of interaction that drives DEG adsorption is hydrogen bonding between the hydroxyl groups of DEG and the CILS ions. The hydrogen-bonding interactions are represented by charge transfer from the lone pair orbital (LP) of an electronegative atom (O and F atoms, here) to the antibonding orbital (σ^*) of a hydrogen bond acceptor (OH and CH). In-line with the thermodynamic results, the positively charged seeds can establish stronger hydrogen-bonding networks with more hydrogen bonds relative to their negatively charged forms. This is somewhat surprising and counterintuitive because simple (e.g., monoatomic) anions are typically better hydrogen bond acceptors than simple cations. This would likely be the case for the isolated EMI/BMI cations and TFMS/BF4/FAP anions alone—however, their composite clusters behave differently. For the EMITFMS and BMIBF4 clusters, DEG actually prefers to bind to the anionic constituents of the clusters partly

because LP(F) to $\sigma^*(OH)_{DEG}$ hydrogen bonding is very effective in DEG adsorption on BMIBF4 and influential on DEG-(EMIFAP)EMI$^+$-1 cluster formation. However, the cations act to stabilize the binding by providing more hydrogen bond acceptors (making the H-bonding network stronger), leading to a positive sign preference. In the case of EMIFAP, DEG actually prefers to adsorb on the cationic constituents because of FAP's inefficiency in acting as a hydrogen-bonding acceptor, which results in the low potency of negative EMIFAP seeds for DEG adsorption. Moreover, the larger size of the FAP anion limits its adsorption ability, relative to the BF4 and TFMS anions, which is consistent with the observations of Maisser and Hogan,[51] whose ion mobility measurements indicated that smaller ions are more efficient in the formation of ion–vapor complexes between n-butanol and the K$^+$, Rb$^+$, Cs$^+$, Br$^-$, and I$^-$ ions under subsaturated conditions. Nevertheless, while the ether oxygen of DEG is not involved in DEG adsorption onto EMITFMS and BMIBF4, it assists DEG stabilization over the EMIFAP's cationic constituents.

After initial DEG adsorption, we studied the growth of the DEG clusters on the CILSs by focusing on the most stable negatively and positively charged IL seeds. Note that these are not always the seeds leading to the best CILS-DEG adsorption ΔG. However, because the "best" conformational composition with respect to DEG adsorption is likely to be different for each number of DEG, we selected the most stable "DEG-free" seeds to keep the comparison consistent. The obtained ΔG values for adsorption of 1-3 DEG molecules are given in Table S1 and the CILS-DEG structures are shown in Figure 4. The charge preference trend seen in Table 3 continues with the addition of additional DEG molecules, corroborating our hypothesis that single-molecule adsorption studies are representative of the whole process. For both the positively and negatively charged EMITFMS and BMIBF4 seeds, nucleation starts by binding of a single DEG molecule to the TFMS and BF4 anions, but subsequent DEG molecules are then bound to the cations. For EMIFAP, the first and subsequent DEG molecules are all bound to the cations. For all CILSs, the intramolecular hydrogen bonding between the DEG molecules further promotes the heterogeneous nucleation process, with the addition of the second DEG molecule often (in 5 of 6 cases) being even more favorable than the first (see Table S1).

CONCLUSION

In general, both experimental and theoretical results indicate that DEG nucleation on the CILSs displays a positive sign preference. The quantum chemical calculations are able to generate CILS models with CCSs very close to that of the experimentally produced seeds. Also, modeling single molecules adsorbing to the smallest possible charged seeds can capture the sign preference and the overall differences in the nucleating abilities of the different ionic liquids. This suggests that such relatively simple model calculations can be

Table 2. Experimental and Modeled CCS (Å^2) and Difference of the Modeled Value Relative to the Experimental Value (%) for CILS Clusters of the Type $(AC)_nA^-$ and $(AC)_nC^+$

	BMIBF4$^-$	BMIBF4$^+$	EMIFTMS$^-$	EMIFTMS$^+$	EMIFAP$^-$	EMIFAP$^-$
model	173.71	193.73	186.82	190.79	249.68	225.49
experiment	172.95	190.49	185.17	181.09	249.05	210.13
difference	0.44	1.70	0.89	5.36	0.25	7.31

Table 3. Thermodynamics of One DEG Molecule Adsorption Considering Quasi-Harmonic Correction (See Section SB of the Supporting Information) at 298.15 K[a]

CILS	ωb97X-D/6-31+G*				ωb97X-D/def2TZVP			
	ΔE	ΔH	ΔG	ΔS	ΔE	ΔH	ΔG	ΔS
(EMITFMS)TFMS⁻	_−94.0_	−95.9	**−28.4**	−226.5	_−83.1_	−83.7	**−17.9**	−220.5
(EMITFMS)EMI⁺	_−104.9_	_−105.3_	**−43.4**	−207.4	_−102.0_	−102.8	**−34.6**	−228.8
(BMIBF4)BF4⁻-1	−86.8	−87.7	−24.2	−212.8	−84.9	−85.6	−19.5	−221.8
(BMIBF4)BF4⁻-2	_−105.4_	_−109.3_	**−37.0**	−242.3	_−89.7_	−90.5	**−21.3**	−232.0
(BMIBF4)BF4⁻-3	−85.3	−86.2	−23.6	−209.9	−82.1	−82.3	−19.5	−210.6
(BMIBF4)BMI⁺-1	−87.0	−87.9	−22.9	−217.9	−82.9	−83.9	−15.6	−228.8
(BMIBF4)BMI⁺-2	−82.6	−84.8	−16.6	−228.8	−80.4	−81.5	−13.5	−228.0
(BMIBF4)BMI⁺-3	−91.8	−93.8	−26.1	−226.8	−87.1	−87.2	−22.4	−217.4
(BMIBF4)BMI⁺-4	−88.8	−90.3	−22.6	−227.0	−86.4	−86.7	−19.5	−225.6
(BMIBF4)BMI⁺-5	_−104.9_	_−106.5_	**−40.2**	−222.2	_−98.8_	−99.7	**−31.9**	−227.5
(BMIBF4)BMI⁺-6	−97.2	−98.3	−32.1	−222.2	−92.7	−92.7	−27.4	−219.1
(EMIFAP)FAP⁻-1	−62.5	−61.9	−0.2	−206.9	_−72.8_	−71.6	**−8.7**	−211.1
(EMIFAP)FAP⁻-2	_−74.6_	−73.9	**−14.2**	−200.0	−71.6	−72.5	−3.6	−231.2
(EMIFAP)FAP⁻-3	−65.4	−64.9	−3.8	−205.0	−66.2	−66.1	−0.9	−218.6
(EMIFAP)EMI⁺-1	_−79.2_	−78.9	**−15.6**	−212.3	_−74.0_	−73.0	**−9.2**	−214.0
(EMIFAP)EMI⁺-2	−77.9	−80.3	−12.1	−228.7	−69.6	−68.5	−4.2	−215.6

[a]The ΔE, ΔH, and ΔG values are in kJ mol⁻¹, while the ΔS values are in J mol⁻¹. The bolded, italicized, and underlined values respectively highlight the most efficient seeds for DEG nucleation based on the ΔG, ΔH, and ΔE criteria.

Table 4. Summary of the Second-Order Perturbation Energies ($E^{(2)}$ Stabilization Energy; kJ mol⁻¹) Related to Charge Transfer from/to DEG NBOs in the Form of NBO Type (atom/bond$_{unit\ moiety}$)$_{unit}$[a]

(EMITFMS)EMI⁺			(EMITFMS)TFMS⁻		
from	to	$E^{(2)}$	from	to	$E^{(2)}$
LP(O$_{OH-1}$)$_{DEG}$	σ*(CN$_{cyc-2}$)$_{EMI-1}$	4.4	LP(O$_{OH-1}$)$_{DEG}$	σ*(CH$_{cyc-1}$)$_{EMI}$	20.7
LP(O$_{OH-2}$)$_{DEG}$	σ*(CH$_{cyc-0}$)$_{EMI-2}$	23.5	LP(O$_{OH-1}$)$_{DEG}$	σ*(CH$_{cyc-1}$)$_{EMI}$	5.1
LP(O$_{OH-2}$)$_{DEG}$	σ*(CH$_{ethyl-1}$)$_{EMI-2}$	5.3	LP(O$_{OS-2}$)$_{TFMS2}$	σ*(OH$_{OH-2}$)$_{DEG}$	48.6
LP(O$_{OS-1}$)$_{TFMS}$	σ*(OH$_{OH-1}$)$_{DEG}$	11.8	LP(O$_{OS-3}$)$_{TFMS2}$	σ*(CH$_{CH-2}$)$_{DEG}$	4.4
LP(O$_{OS-1}$)$_{TFMS}$	σ*(OH$_{OH-2}$)$_{DEG}$	9.2	σ*(OS$_{OS-2}$)$_{TFMS2}$	σ*(OH$_{OH-2}$)$_{DEG}$	8.4
LP(O$_{OS-1}$)$_{TFMS}$	σ*(OH$_{OH-1}$)$_{DEG}$	14.5	σ*(OS$_{OS-3}$)$_{TFMS2}$	σ*(CH$_{CH-1}$)$_{DEG}$	7.8
LP(O$_{OS-1}$)$_{TFMS}$	σ*(OH$_{OH-2}$)$_{DEG}$	12.0			
LP(O$_{OS-1}$)$_{TFMS}$	σ*(OH$_{OH-1}$)$_{DEG}$	10.0			
LP(O$_{OS-1}$)$_{TFMS}$	σ*(OH$_{OH-2}$)$_{DEG}$	11.6			
(BMIBF4)BMI⁺-5			**(BMIBF4)BF4⁻-3**		
from	to	$E^{(2)}$	from	to	$E^{(2)}$
LP(O$_{OH-1}$)$_{DEG}$	σ*(CH$_{cyc-0}$)$_{BMI-1}$	5.6	LP(O$_{OH-1}$)$_{DEG}$	σ*(CH$_{methyl}$)$_{BMI}$	5.5
LP(O$_{OH-1}$)$_{DEG}$	σ*(CH$_{cyc-0}$)$_{BMI-1}$	31.3	LP(F$_{BF-3}$)$_{BF4-1}$	σ*(OH$_{OH-2}$)$_{DEG}$	8.0
LP(O$_{OH-2}$)$_{DEG}$	σ*(CH$_{cyc-0}$)$_{BMI-2}$	9.8	LP(F$_{BF-3}$)$_{BF4-1}$	σ*(OH$_{OH-2}$)$_{DEG}$	46.6
LP(O$_{OH-2}$)$_{DEG}$	σ*(CH$_{butyl-1}$)$_{BMI-1}$	7.7			
LP(O$_{OH-2}$)$_{DEG}$	σ*(CH$_{cyc-0}$)$_{BMI-2}$	15.1			
LP(F$_{BF-3}$)$_{BF4}$	σ*(OH$_{OH-1}$)$_{DEG}$	9.3			
LP(F$_{BF-3}$)$_{BF4}$	σ*(OH$_{OH-2}$)$_{DEG}$	6.3			
LP(F$_{BF-3}$)$_{BF4}$	σ*(OH$_{OH-1}$)$_{DEG}$	13.5			
LP(F$_{BF-3}$)$_{BF4}$	σ*(OH$_{OH-2}$)$_{DEG}$	9.3			
LP(F$_{BF-3}$)$_{BF4}$	σ*(OH$_{OH-1}$)$_{DEG}$	11.6			
LP(F$_{BF-3}$)$_{BF4}$	σ*(OH$_{OH-2}$)$_{DEG}$	17.4			
(EMIFAP)EMI⁺-1			**(EMIFAP)FAP⁻-1**		
from	to	$E^{(2)}$	from	to	$E^{(2)}$
LP(O$_O$)$_{DEG}$	σ*(CH$_{cyc-0}$)$_{EMI-1}$	5.8	LP(O$_O$)$_{DEG}$	σ*(CH$_{cyc-0}$)$_{EMI}$	9.4
LP(O$_{O-2}$)$_{DEG}$	σ*(CH$_{cyc-0}$)$_{EMI-1}$	17.4	LP(O$_O$)$_{DEG}$	σ*(CH$_{cyc-0}$)$_{EMI}$	6.7
LP(F$_{PF-1}$)$_{FAP}$	σ*(OH$_{OH-2}$)$_{DEG}$	8.9			

[a]A threshold of 1 kcal mol⁻¹ (=4.2 kJ mol⁻¹) has been used (i.e., interactions with smaller perturbation energies are not reported). The units and unit moieties are numbered to make them distinguishable. "cyc" represents the imidazolium ring of EMI and BMI. The hydroxyl and ether oxygen atoms of DEG are distinguished as O$_{OH}$ and O$_O$, respectively.

immensely useful in predicting and explaining nucleation of complex seed−vapor mixtures. The experimentally observed

differences between the CILSs are caused by the hydrogen-bonding patterns. For example, positive seeds tend to form
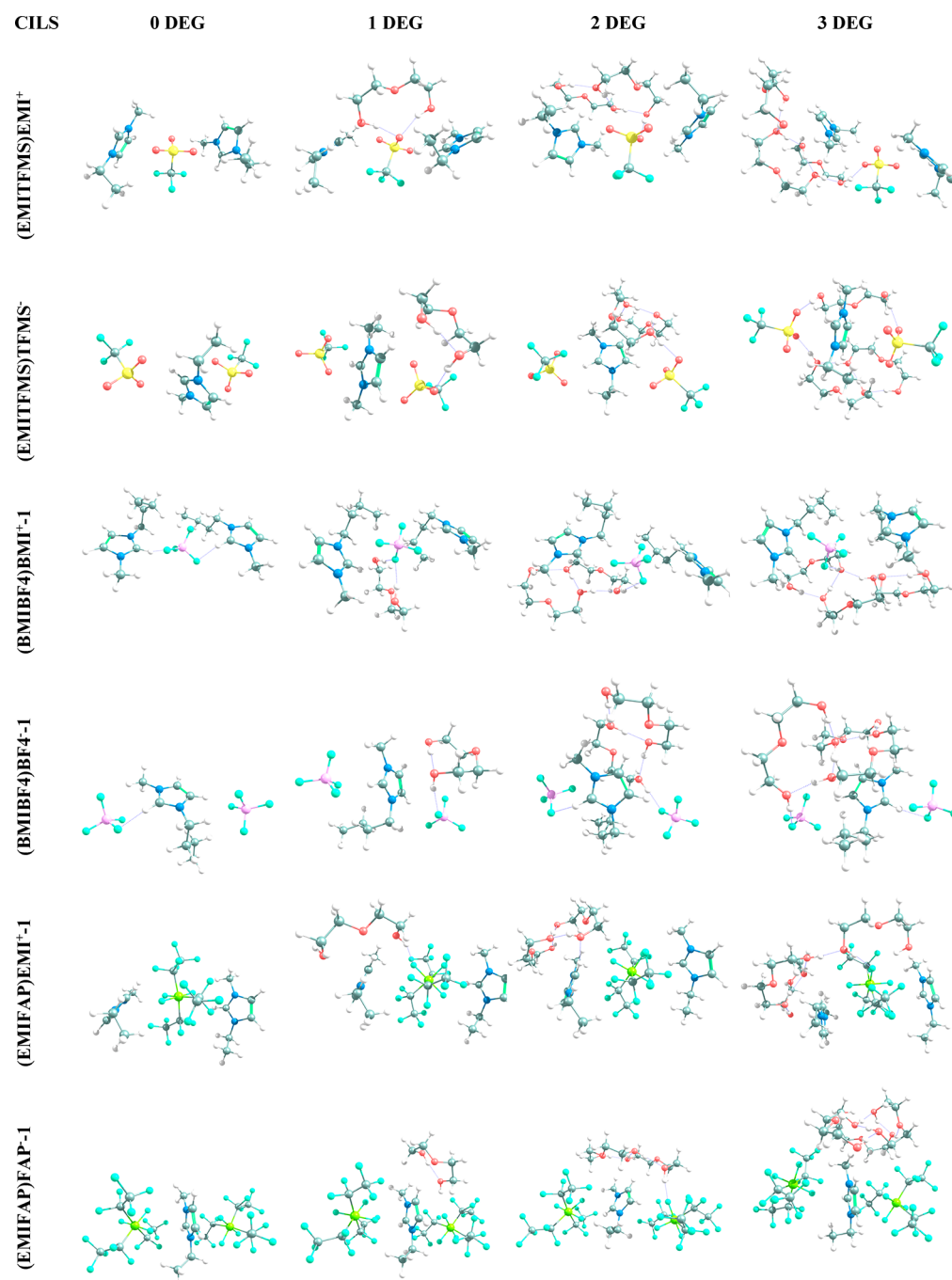
Figure 4. Starting steps of DEG nucleation on the CILSs at 298.15 K and the ωb97X-D/6-31+G* level of theory. The viewing angles are chosen to best clarify the interaction networks. The blue dotted lines represent the hydrogen bonds.

both stronger and more numerous hydrogen bonds with DEG. This leads to lower adsorption free energies, and consequently lower onset supersaturations for heterogeneous nucleation onto the cationic seeds.

■ ASSOCIATED CONTENT

Ⓢ Supporting Information

The Supporting Information is available free of charge at https://pubs.acs.org/doi/10.1021/acs.jpcc.0c09481.

Schematic presentation of the experimental setup, details of the computational method, structures of the ionic liquids, diethylene glycol, the selected anion/cation conformers/configurations and the CILSs, effect of

conformational/configurational diversity on the CILSs, adsorption energies for the addition of two and three DEG molecules to the CILSs, and the CHelpG atomic charges of all CILSs (PDF)

Geometry and frequencies (output files) of all seeds and DEG-CILS complexes (ZIP)

■ AUTHOR INFORMATION

Corresponding Authors

Juha Kangasluoma − *Institute for Atmospheric and Earth System Research/Physics, Faculty of Science, University of Helsinki, Helsinki 00014, Finland; Aerosol and Haze Laboratory, Beijing Advanced Innovation Center for Soft*

Matter Science and Engineering, Beijing University of Chemical Technology, Beijing 100029, China; ● orcid.org/0000-0002-1639-1187; Email: juha.kangasluoma@helsinki.fi

Fatemeh Keshavarz − *Institute for Atmospheric and Earth System Research/Physics, Faculty of Science, University of Helsinki, Helsinki 00014, Finland;* ● orcid.org/0000-0003-2189-7809; Email: fatemeh.keshavarz@helsinki.fi

Authors

    Jakub Kubečka − *Institute for Atmospheric and Earth System Research/Physics, Faculty of Science, University of Helsinki, Helsinki 00014, Finland;* ● orcid.org/0000-0002-8002-0911

    Michel Attoui − *Laboratoire Interuniversitaire des Systèmes Atmosphériques, UMR CNRS 7583, Université Paris Est Créteil et Université de Paris, Institut Pierre Simon Laplace, Créteil 94010, France*

    Hanna Vehkamäki − *Institute for Atmospheric and Earth System Research/Physics, Faculty of Science, University of Helsinki, Helsinki 00014, Finland;* ● orcid.org/0000-0002-5018-1255

    Theo Kurtén − *Department of Chemistry, Faculty of Science, University of Helsinki, Helsinki FI-00014, Finland;* ● orcid.org/0000-0002-6416-4931

Complete contact information is available at:
https://pubs.acs.org/10.1021/acs.jpcc.0c09481

Author Contributions

[#]F.K. and J.K. contributed equally to this work.

Notes

The authors declare no competing financial interest.

■ **REFERENCES**

(1) Murty, B. S.; Kori, S. A.; Chakraborty, M. Grain Refinement of Aluminium and Its Alloys by Heterogeneous Nucleation and Alloying. *Int. Mater. Rev.* **2002**, *47*, 3−29.

(2) Zhai, W. T.; Yu, J.; Wu, L. C.; Ma, W. M.; He, J. S. Heterogeneous Nucleation Uniformizing Cell Size Distribution in Microcellular Nanocomposites Foams. *Polymer* **2006**, *47*, 7580−7589.

(3) Zhao, J. J.; Wang, M. H.; Jebutu, M. S.; Zhu, M. H.; Gleason, K. K. Fundamental Nanoscale Surface Strategies for Robustly Controlling Heterogeneous Nucleation of Calcium Carbonate. *J. Mater. Chem. A* **2019**, *7*, 17242−17247.

(4) Meng, Q.; Deng, B.; Zhang, H.; Wang, B.; Zhang, W.; Wen, Y.; Ming, H.; Zhu, X.; Guan, Y.; Xiang, Y.; et al. Heterogeneous Nucleation and Growth of Electrodeposited Lithium Metal on the Basal Plane of Single-Layer Graphene. *Energy Storage Mater.* **2019**, *16*, 419−425.

(5) Murray, B. J.; Wilson, T. W.; Dobbie, S.; Cui, Z.; Al-Jumur, S. M.; Möhler, O.; Schnaiter, M.; Wagner, R.; Benz, S.; Niemand, M.; et al. Heterogeneous Nucleation of Ice Particles on Glassy Aerosols under Cirrus Conditions. *Nat. Geosci.* **2010**, *3*, 233−237.

(6) Zuberi, B.; Bertram, A. K.; Cassa, C. A.; Molina, L. T.; Molina, M. J. Heterogeneous Nucleation of Ice in $(NH_4)(2)SO_4$−H_2O Particles with Mineral Dust Immersions. *Geophys. Res. Lett.* **2002**, *29*, 142-1.

(7) Jun, Y. S.; Kim, D.; Neil, C. W. Heterogeneous Nucleation and Growth of Nanoparticles at Environmental Interfaces. *Acc. Chem. Res.* **2016**, *49*, 1681−1690.

(8) Park, Y.; Wyslouzil, B. E. CO_2 Condensation onto Alkanes: Unconventional Cases of Heterogeneous Nucleation. *Phys. Chem. Chem. Phys.* **2019**, *21*, 8295−8313.

(9) Page, A. J.; Sear, R. P. Heterogeneous Nucleation in and out of Pores. *Phys. Rev. Lett.* **2006**, *97*, 065701−065704.

(10) Varanasi, K. K.; Hsu, M.; Bhate, N.; Yang, W. S.; Deng, T. Spatial Control in the Heterogeneous Nucleation of Water. *Appl. Phys. Lett.* **2009**, *95*, 094101−094103.

(11) Winkler, P. M.; Steiner, G.; Vrtala, A.; Vehkamaki, H.; Noppel, M.; Lehtinen, K. E. J.; Reischl, G. P.; Wagner, P. E.; Kulmala, M. Heterogeneous Nucleation Experiments Bridging the Scale from Molecular Ion Clusters to Nanoparticles. *Science* **2008**, *319*, 1374−1377.

(12) Kangasluoma, J.; Samodurov, A.; Attoui, M.; Franchin, A.; Junninen, H.; Korhonen, F.; Kurtén, T.; Vehkamäki, H.; Sipilä, M.; Lehtipalo, K.; et al. Heterogeneous Nucleation onto Ions and Neutralized Ions: Insights into Sign-Preference. *J. Phys. Chem. C* **2016**, *120*, 7444−7450.

(13) Winkler, P. M.; Hienola, A.; Steiner, G.; Hill, G.; Vrtala, A.; Reischl, G. P.; Kulmala, M.; Wagner, P. E. Effects of Seed Particle Size and Composition on Heterogeneous Nucleation of N-Nonane. *Atmos. Res.* **2008**, *90*, 187−194.

(14) Tauber, C.; Chen, X. S.; Wagner, P. E.; Winkler, P. M.; Hogan, C. J.; Maisser, A. Heterogeneous Nucleation onto Monoatomic Ions: Support for the Kelvin-Thomson Theory. *ChemPhysChem* **2018**, *19*, 3144−3149.

(15) Winkler, P. M.; Steiner, G.; Vrtala, A.; Reischl, G. P.; Kulmala, M.; Wagner, P. E. Unary and Binary Heterogeneous Nucleation of Organic Vapors on Monodisperse Wox Seed Particles with Diameters Down to 1.4 Nm. *Aerosol Sci. Technol.* **2011**, *45*, 493−498.

(16) Iida, K.; Stolzenburg, M. R.; McMurry, P. H. Effect of Working Fluid on Sub-2 nm Particle Detection with a Laminar Flow Ultrafine Condensation Particle Counter. *Aerosol Sci. Technol.* **2009**, *43*, 81−96.

(17) Tauber, C.; Steiner, G.; Winkler, P. M. Counting Efficiency Determination from Quantitative Intercomparison between Expansion and Laminar Flow Type Condensation Particle Counter. *Aerosol Sci. Technol.* **2019**, *53*, 344−354.

(18) Kupc, A.; Winkler, P. M.; Vrtala, A.; Wagner, P. Unusual Temperature Dependence of Heterogeneous Nucleation of Water Vapor on Ag Particles. *Aerosol Sci. Technol.* **2013**, *47*, i−iv.

(19) Oberreit, D. R.; McMurry, P. H.; Hogan, C. J. Analysis of Heterogeneous Uptake by Nanoparticles Via Differential Mobility Analysis-Drift Tube Ion Mobility Spectrometry. *Phys. Chem. Chem. Phys.* **2014**, *16*, 6968−6979.

(20) Nasibulin, A. G.; Fernandez de la Mora, J.; Kauppinen, E. I. Ion-Induced Nucleation of Dibutyl Phthalate Vapors on Spherical and Nonspherical Singly and Multiply Charged Polyethylene Glycol Ions. *J. Phys. Chem. A* **2008**, *112*, 1133−1138.

(21) Schobesberger, S.; Winkler, P. M.; Pinterich, T.; Vrtala, A.; Kulmala, M.; Wagner, P. E. Experiments on the Temperature Dependence of Heterogeneous Nucleation on Nanometer-Sized Nacl and Ag Particles. *ChemPhysChem* **2010**, *11*, 3874−3882.

(22) Seto, T.; Okuyama, K.; de Juan, L.; Fernandéz de la Mora, J. Condensation of Supersaturated Vapors on Monovalent and Divalent Ions of Varying Size. *J. Chem. Phys.* **1997**, *107*, 1576−1585.

(23) Gamero-Castano, M.; Fernandéz de la Mora, J. Ion-Induced Nucleation: Measurement of the Effect of Embryo's Size and Charge State on the Critical Supersaturation. *J. Chem. Phys.* **2002**, *117*, 3345−3353.

(24) Fernandéz de la Mora, J. Heterogeneous Nucleation with Finite Activation Energy and Perfect Wetting: Capillary Theory Versus Experiments with Nanometer Particles, and Extrapolations on the Smallest Detectable Nucleus. *Aerosol Sci. Technol.* **2011**, *45*, 543−554.

(25) Wilson, C. T. R. IX. On the Condensation Nuclei Produced in Gases by the Action of Röntgen Rays, Uranium Rays, Ultra-Violet Light, and Other Agents. *Phil. Trans. R. Soc. Lond. A* **1899**, *192*, 403−453.

(26) Kane, D.; Daly, G. M.; El-Shall, S. Condensation of Supersaturated Vapors on Benzene Ions Generated by Resonant Two-Photon Ionization: A New Technique for Ion Nucleation. *J. Phys. Chem.* **1995**, *99*, 7867−7870.

(27) Adachi, M.; Okuyama, K.; Seinfeld, J. H. Experimental Studies on Ion-Induced Nucleation. *J. Aerosol Sci.* **1992**, *23*, 327−337.

(28) Katz, J. L.; Fisk, J. A.; Chakarov, V. M. Condensation of a Supersaturated Vapor Ix. Nucleation on Ions. *J. Chem. Phys.* **1994**, *101*, 2309−2318.

(29) Rabeony, H.; Mirabel, P. Experimental Study of Vapor Nucleation on Ions. *J. Phys. Chem.* **1987**, *91*, 1815−1818.

(30) Abdelsayed, V.; Samy El-Shall, M. Vapor Phase Nucleation on Neutral and Charged Nanoparticles: Condensation of Supersaturated Trifluoroethanol on Mg Nanoparticles. *J. Chem. Phys.* **2007**, *126*, 024706.

(31) Abdelsayed, V.; Samy El-Shall, M. Direct Observation of Metal Nanoparticles as Heterogeneous Nuclei for the Condensation of Supersaturated Organic Vapors: Nucleation of Size-Selected Aluminum Nanoparticles in Acetonitrile and N-Hexane Vapors. *J. Chem. Phys.* **2014**, *141*, 054710.

(32) Sipilä, M.; Lehtipalo, K.; Attoui, M.; Neitola, K.; Petaja, T.; Aalto, P. P.; O'Dowd, C. D.; Kulmala, M. Laboratory Verification of Ph-Cpc's Ability to Monitor Atmospheric Sub-3 nm Clusters. *Aerosol Sci. Technol.* **2009**, *43*, 126−135.

(33) Kuang, C. A.; Chen, M. D.; McMurry, P. H.; Wang, J. Modification of Laminar Flow Ultrafine Condensation Particle Counters for the Enhanced Detection of 1 Nm Condensation Nuclei. *Aerosol Sci. Technol.* **2012**, *46*, 309−315.

(34) Gamero-Castano, M.; Fernandéz de la Mora, J. A Condensation Nucleus Counter (CNC) Sensitive to Singly Charged Sub-Nanometer Particles. *J. Aerosol Sci.* **2000**, *31*, 757−772.

(35) Kangasluoma, J.; Kuang, C.; Wimmer, D.; Rissanen, M. P.; Lehtipalo, K.; Ehn, M.; Worsnop, D. R.; Wang, J.; Kulmala, M.; Petaja, T. Sub-3 nm Particle Size and Composition Dependent Response of a Nano-Cpc Battery. *Atmos. Meas. Tech.* **2014**, *7*, 689−700.

(36) Kangasluoma, J.; Junninen, H.; Lehtipalo, K.; Mikkila, J.; Vanhanen, J.; Attoui, M.; Sipila, M.; Worsnop, D.; Kulmala, M.; Petaja, T. Remarks on Ion Generation for CPC Detection Efficiency Studies in Sub-3-nm Size Range. *Aerosol Sci. Technol.* **2013**, *47*, 556−563.

(37) Kathmann, S. M.; Schenter, G. K.; Garrett, B. C. Ion-Induced Nucleation: The Importance of Chemistry. *Phys. Rev. Lett.* **2005**, *94*, 116104.

(38) Oh, K. J.; Gao, G. T.; Zeng, X. C. Nucleation of Water and Methanol Droplets on Cations and Anions: The Sign Preference. *Phys. Rev. Lett.* **2001**, *86*, 5080−5083.

(39) Nadykto, A. B.; Yu, F. Q.; Herb, J. Towards Understanding the Sign Preference in Binary Atmospheric Nucleation. *Phys. Chem. Chem. Phys.* **2008**, *10*, 7073−7078.

(40) Kurten, T.; Ortega, I. K.; Vehkamaki, H. The Sign Preference in Sulfuric Acid Nucleation. *J. Mol. Struct.: THEOCHEM* **2009**, *901*, 169−173.

(41) Kangasluoma, J.; Hering, S.; Picard, D.; Lewis, G.; Enroth, J.; Korhonen, F.; Kulmala, M.; Sellegri, K.; Attoui, M.; Petaja, T. Characterization of Three New Condensation Particle Counters for Sub-3 nm Particle Detection During the Helsinki CPC Workshop: The Adi Versatile Water CPC, Tsi 3777 Nano Enhancer and Boosted Tsi 3010. *Atmos. Meas. Tech.* **2017**, *10*, 2271−2281.

(42) Larriba, C.; Hogan, C. J.; Attoui, M.; Borrajo, R.; Garcia, J. F.; de la Mora, J. F. The Mobility-Volume Relationship Below n.0 Nm Examined by Tandem Mobility-Mass Measurement. *Aerosol Sci. Technol.* **2011**, *45*, 453−467.

(43) Frisch, M. J.; Trucks, G. W.; Schlegel, H. B.; Scuseria, G. E.; Robb, M. A.; Cheeseman, J. R.; Scalmani, G.; Barone, V.; Petersson, G. A.; Nakatsuji, H.; et al. *Gaussian 16*, Rev. A.01; Gaussian, Inc.: Wallingford, CT, 2016.

(44) Grimme, S. Supramolecular Binding Thermodynamics by Dispersion-Corrected Density Functional Theory. *Chem. - Eur. J.* **2012**, *18*, 9955−9964.

(45) Chon, N. L.; Lee, S. H.; Lin, H. A Theoretical Study of Temperature Dependence of Cluster Formation from Sulfuric Acid and Ammonia. *Chem. Phys.* **2014**, *433*, 60−66.

(46) Funes-Ardoiz, I.; Paton, R. S. *GoodVibes: GoodVibes* V1.0.1. 2016. https://zenodo.org/record/60811.

(47) Kubecka, J.; Besel, V.; Kurten, T.; Myllys, N.; Vehkamaki, H. Configurational Sampling of Noncovalent (Atmospheric) Molecular Clusters: Sulfuric Acid and Guanidine. *J. Phys. Chem. A* **2019**, *123*, 6022−6033.

(48) Coots, J.; Gandhi, V.; Onakoya, T.; Chen, X.; Larriba-Andaluz, C. A Parallelized Tool to Calculate the Electrical Mobility of Charged Aerosol Nanoparticles and Ions in the Gas Phase. *J. Aerosol Sci.* **2020**, *147*, 105570−105576.

(49) Larriba, C.; Hogan, C. J. Momentum Transfer Collision Cross Sections and Ion Mobilities in Diatomic Gases: Measurement Vs. Prediction with Non-Specular Scattering Models. *J. Phys. Chem. A* **2013**, *117*, 3887−3901.

(50) Shrivastav, V. R. *Optimization of Lennard-Jones Potential Parameters and Benchmark Comparison between Ion Mobility Calculators in Free Molecular Regime*. PhD Thesis, Purdue University, 2017.

(51) Maisser, A.; Hogan, C. J. Examination of Organic Vapor Adsorption onto Alkali Metal and Halide Atomic Ions by Using Ion Mobility Mass Spectrometry. *ChemPhysChem* **2017**, *18*, 3039−3046.